Optics Communications 426 (2018) 170–181

Contents lists available at ScienceDirect

Optics Communications

journal homepage: www.elsevier.com/locate/optcom

# A novel super-resolution imaging method based on TDI CCD charge transfer and random exposure

Yun-Hui Li [a,b,*], Xiao-Dong Wang [a], Zhi Wang [a,c]

[a] Changchun Institute of Optics, Fine Mechanics and Physics, Chinese Academy of Sciences, Changchun 130033, China
[b] University of Chinese Academy of Sciences, Beijing 100049, China
[c] Changchun UP Optotech (Holding) Co., Ltd, Changchun 130033, China

ARTICLE INFO

*Keywords:*
Super-resolution
Computational imaging
Compressed sensing
Imaging reconstruction

ABSTRACT

Based on compressed sensing theory and TDI CCD driving mode, a collaborative coding method founded on TDI CCD charge transfer and random exposure is proposed in this paper, which breaks through the limitation of pixel size and achieves the improvement of one-dimensional image resolution. By extending this method, an orthogonal dual detector super-resolution imaging system is established, which realizes the improvement of two-dimensional image resolution. Further, the convex optimization algorithm and the proportional fusion algorithm are proposed as the two-dimensional image fusion algorithm. Theoretical modeling and simulation results demonstrate the effectiveness of the proposed imaging method and system, which provide an innovative approach of system implementation for super-resolution imaging based on compressed sensing theory.

## 1. Introduction

The Nyquist–Shannon sampling theorem specifies that if a signal is to be completely sampled without any loss of information, it is required to use a sampling frequency at least twice the signal bandwidth. In the actual optical imaging system, the enhancement of imaging resolution depends on two factors: the front-end optical system and the back-end image detector. The front-end optical system is limited by the diffraction limit, and the back-end detector sampling is constrained by the Shannon sampling theorem. For high-resolution and large-scale imaging, a detector with smaller pixel size and larger number of pixels is needed, which is difficult to achieve due to the limitation of the detector manufacturing process. Meanwhile, massive data brings a heavy burden to the data storage and transmission of the hardware system.

The compressed sensing (CS) theory proposed by E. J. Candès, J. Romberg, T. Tao and D. L. Donoho et al. in 2006 provides a new path to solve this problem [1–5]. E. J. Candès et al. proved that if a signal is sparse in a transform domain, the original signal can be recovered with a high probability through a small amount of projection of the signal in other unrelated transform domain. This breaks through the limitation of Nyquist–Shannon sampling theorem, subverts the traditional one-to-one imaging mode, and greatly reduces the hardware requirements of the signal acquisition devices. Therefore, it has been widely concerned in the fields of remote sensing, medical imaging, radar imaging and wireless communication in recent years [6–9].

In order to meet the demand of signal aliasing sampling in the compressed sensing theory, several hardware implementations have been proposed by scholars, including single pixel camera based on Digital Micro-mirror Device (DMD) [10–15], Complementary Metal Oxide Semiconductor (CMOS) image sensor with compressed sensing sampling mode [16,17], coded aperture [18–20], random active illumination [21,22], moving random exposure and so on [23].

As one of the most typical applications of compressed sensing theory, single pixel camera based on DMD uses single pixel detector instead of image sensor to complete the image acquisition, which greatly reduces the cost and the complexity of the hardware design [10,11]. However, when large-scale imaging is performed, the number of coding increases, resulting in a sharp increase in the time of observation. As an improvement of the above system, John P. Dumas and A. Sankaranarayanan proposed an architecture for plane-coded computational imaging that is based on a highly parallel version of the single pixel camera which reduces the encoding time, thus improving real-time performance of the system [12,13]. Further, a complementary modulation to improve the performance of the observation matrix was proposed by Wen-Kai Yu, thereby improving the quality of image restoration [14]. However, the above methods are all based on DMD for encoding. Although the requirements for detector pixel size and number of pixels are reduced, they are passed on to the DMD and the resolution of the image depends on the DMD, where there are also constraints on the size and number of micro-mirrors.

* Corresponding author at: Changchun Institute of Optics, Fine Mechanics and Physics, Chinese Academy of Sciences, Changchun 130033, China.
*E-mail address:* liyunhui_ciomp@126.com (Y.-H. Li).

https://doi.org/10.1016/j.optcom.2018.05.044
Received 10 April 2018; Received in revised form 9 May 2018; Accepted 13 May 2018
Available online 26 May 2018

L. Jacques presented a CMOS imager to perform compressed sensing coding by random convolution, which is achieved by a shift register set in a pseudo-random configuration [16]. In order to reduce the complexity of the pseudo-random sequence generating circuits and reconstruction algorithm, the whole system was divided into several sub blocks by Huixian Ye, each of which contains a single sigma-delta Analog to Digital Converter (ADC) [17]. However, the encoding method based on CMOS sensor is essentially the compressed processing of the output signal, which surely reduces the burden on the subsequent ADC and data transmission and storage. But it has no effect on the front-end detector and therefore cannot solve the problem from the source.

Computational imaging based on multi-aperture optics turns the encoding in the time dimension into the spatial dimension, which greatly shortens the encoding time. But the system with complicated structure is difficult to implement [18]. Pawan K. Baheti presented a compressed imaging system based on the use of structured light, where illumination patterns are defined using binary-valued random vectors [21]. Milad I demonstrated that binary illumination based on spatially random distributions provides superior imaging capabilities at high compression ratios [22]. Nevertheless, its applications may be limited because of the random active illumination. Edson Mojica presented a method for the design of high-resolution coded apertures for compressive sensing computed tomography [23]. M. Marquez aimed at reconstructing a high-resolution (HR) spectral images from low-resolution (LR) compressive measurements by solving a single convex optimization problem based on the fusion of CS and super-resolution techniques [24]. Guangming Shi introduced a high-resolution imaging method based on moving random exposure. Compressive measurements are made by a low-resolution camera with randomly fluttering shutter, which achieves the improvement of one-dimensional resolution [25].

In this paper, a collaborative coding method based on Time Delay Integration (TDI) Charge Coupled Device (CCD) charge transfer and random exposure is proposed. Compared with the moving random exposure method proposed in Ref. [25], the charge transfer driving is used instead of the camera motion control to achieve more flexible and accurate control. By adjusting the driving timing and random exposure of TDI CCD, one-dimensional compressed sensing imaging under different super-resolution indexes can be realized. Based on the above imaging method, we present an orthogonal dual detector super-resolution imaging system. And two image fusion algorithms based on this system are proposed to achieve the two-dimensional super-resolution image restoration. Two significant innovations are presented in this paper:

(1) Based on compressed sensing theory and TDI CCD driving mode, a collaborative coding method founded on TDI CCD charge transfer and random exposure is proposed in this paper, which breaks through the limitation of pixel size and achieves the improvement of one-dimensional image resolution.

(2) By expanding the above method, an orthogonal dual detector super-resolution imaging system is established, which realizes the improvement of two-dimensional image resolution. In the part of two-dimensional image fusion algorithm, we propose the convex optimization algorithm and the proportional fusion algorithm.

Theoretical modeling and simulations demonstrate the effectiveness of the proposed imaging method and system, which provide an innovative approach of system implementation for super-resolution imaging based on compressed sensing theory.

## 2. Compressed sensing theory

Compressed sensing theory is based on the signal sparsity within a transform domain. Because most of the natural scenes have sparse characteristics in a specific transform domain, the subsampled reconstruction of the original signal can be realized by this theory, which lays a theoretical foundation for super-resolution imaging.

The signal processing flow of the compressed sensing theory is shown in Fig. 1, wherein $X$ is the original signal, which can be sparsely

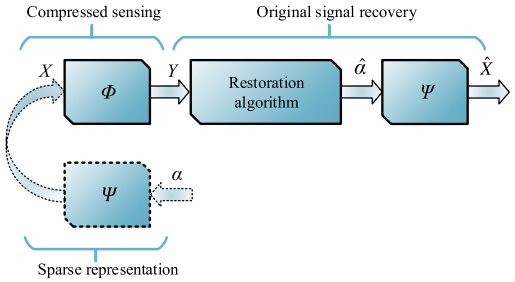


**Fig. 1.** The signal processing flow of the compressed sensing theory.

expressed as $\alpha$ under the transform base $\psi$, $\Phi$ is the measurement matrix, and $Y$ is the observation result. The whole process can be divided into two stages: compressed sensing and original signal recovery. Compressed sensing process can be expressed as:

$$Y = \Phi X = \Phi\Psi\alpha. \tag{1}$$

After the observation result $Y$ is obtained, the sparse representation $\alpha$ of the original signal needs to be iteratively calculated by the restoration algorithm, and the product of the sparse representation $\alpha$ and transform basis $\psi$ is the original signal. This process is called original signal recovery. The restoration algorithm is usually implemented by solving the following optimization problem [1–4]:

$$\hat{\alpha} = \arg\min \|\alpha\|_1 \quad s.t.\ Y = \Phi\Psi\alpha \tag{2}$$

where the symbol $\| \|_1$ represents the $l_1$ norm. The following mainly focuses on the system implementation method of compressed sensing process.

## 3. Coding method based on TDI CCD charge transfer and random exposure

### 3.1. TDI CCD charge transfer mode

Compared with the traditional linear array CCD, TDI CCD adopts the method of time delay integration, which realizes multiple exposures to the same target by driving the charge transfer in synchronization with the target image motion. Therefore, the exposure time has been effectively increased, making TDI CCD has the advantages of high sensitivity and wide dynamic range, so it has been widely applied in space remote sensing, glimmer night vision and other related fields [26–28].

TDI CCD can be divided into two-phase, three-phase and four-phase according to its charge transfer driving mode, all of which have the same basic working principle. The internal structure diagram of the three-phase TDI CCD is shown in Fig. 2, in which the driving signal is mainly composed of the vertical transfer signal CI, the horizontal readout signal CR, and the transfer gate signal TCK. When TDI CCD is used for imaging, the line frequency of the charge transfer is calculated based on the current image motion parameter, so as to realize image motion matching. Then the vertical transfer of charge is accomplished by the signal CI according to the line frequency above. When a row of charge is completely transferred to the horizontal shift register, it will be quantized and output one by one, driven by the signal CR.

The transfer process of the charge between adjacent rows is implemented in multiple steps. Assuming that the TDI CCD is an $n$-phase device, it will take a total of $2n$ steps to complete the transfer of a row of charge if single and dual step driving method is used in a line period. Taking three-phase TDI CCD for example, the timing of the driving signal is shown in Fig. 3. Compared with the traditional burst transfer mode, Fig. 3 shows a new continuous transfer mode, in which the charge

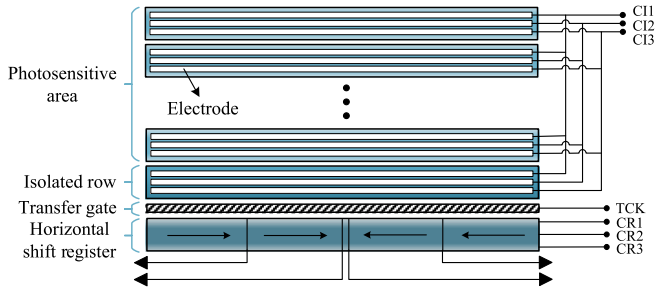


**Fig. 2.** The internal structure diagram of the three-phase TDI CCD.

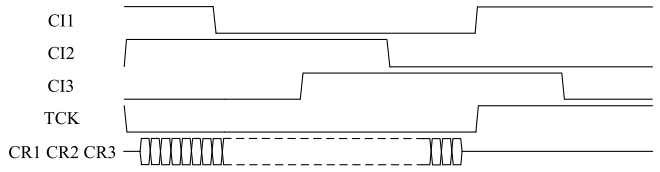


**Fig. 3.** The timing diagram of three-phase TDI CCD.

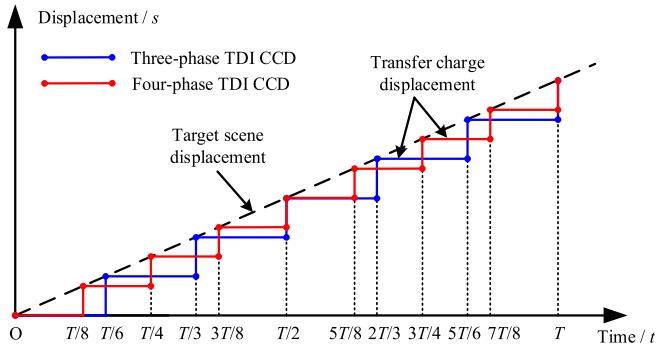


**Fig. 4.** The charge transfer displacement curves of TDI CCD.

transfer image motion is effectively reduced, and therefore has been widely used in recent years.

On the premise of image motion matching, the charge transfer displacement curves of TDI CCD are shown in Fig. 4 when the continuous transfer mode is applied. Wherein the dotted line is the target displacement curve, and $T$ is the line period of charge transfer. It can be seen from the figure that when an $n$-phase TDI CCD is used, a total of $2n$ steps of charge transfer is needed in a line period $T$, and the displacement of each charge transfer step is $1/2n$ pixel size, which provides the possibility of sub-pixel super-resolution imaging.

### 3.2. Collaborative coding method

In traditional applications, each charge packet in TDI CCD moves synchronously with the target scene. A transfer charge packet is all exposed to the same target point throughout the process, thus the final output is the image information of this specific point. While the compressed sensing theory requires coding and observation of the target, for completing the aliased sampling of the target information. Therefore, the observation process requires two conditions: random coding and relative motion.

Compared with traditional applications, TDI CCD is used here for gaze imaging mode instead of push-broom imaging mode, where the detector remains relatively stationary with the target scene, so that the vertically transferred charge packet has relative motion with the target scene. Random coding is implemented with the fast flash exposure of the

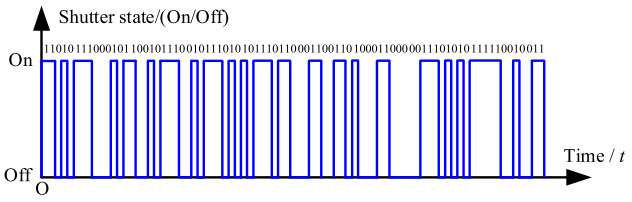


**Fig. 5.** The diagram of random exposure sequence with 0 and 1.

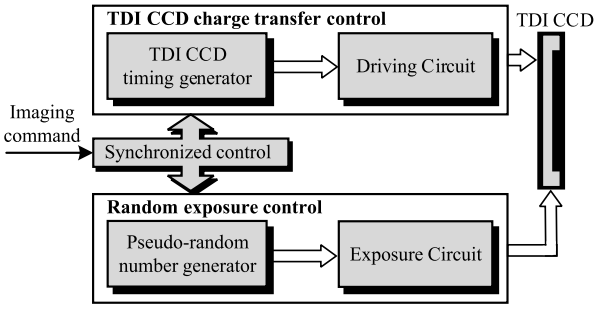


**Fig. 6.** The system block diagram of the collaborative coding method.

electronic shutter, which enables binary coding of 0 and 1. The random exposure sequence is shown in Fig. 5, where "On" indicates the shutter is open, then the corresponding element of the measurement matrix is 1, and "Off" indicates the shutter is closed, then the corresponding element of the measurement matrix is 0.

It is necessary to coordinate the charge transfer with the shutter exposure during the whole compressed coding process. Fig. 6 shows the system block diagram of the collaborative coding method. The driving of the detector is mainly realized by the TDI CCD charge transfer control module and the random exposure control module, where both of them need to be synchronized and coordinated under the control of the imaging command. Synchronized control means that the charge is exposed once when one or multi step of the charge transfer is executed.

### 3.3. Mathematical model established

Assuming that the TDI CCD is an $n$-phase device with the integral number $m$, and a total of $k$ rows of observed data are read out during the entire observation process. The total process can be subdivided into $R$ steps based on a row of charge transfer needs $2n$ steps:

$$R = 2n \cdot (m + k) - 1. \tag{3}$$

The schematic diagram of the collaborative coding process based on charge transfer and random exposure is shown in Fig. 7. For simplified analysis, a column of pixels in the detector is taken as an example, where $\Delta t$ is the time required for one step of charge transfer. Once the charge is transferred one step, the shutter is exposed once for encoding, and the whole process lasts for a period of $R \times \Delta t$. At the beginning of the charge transfer, the output data is discarded due to the fact that the whole scene is not completely exposed to the readout charge, resulting in insufficient information contained in the charge. After the time $2n \times m \times \Delta t$, the data starts to be effectively processed. Each interval of $2n \times \Delta t$ time, one row of charges is completely removed and the data is quantified and read out once. The process continues until $[2n \times (m+k) - 1] \times \Delta t$ moment, and a total of $k$ rows of effective data are read out, and the entire coding observation process is completed.

The above description is the case of one step of charge transfer corresponding to one exposure of the shutter. In practical process, it can be the charge transfers one step corresponding to once exposure, or

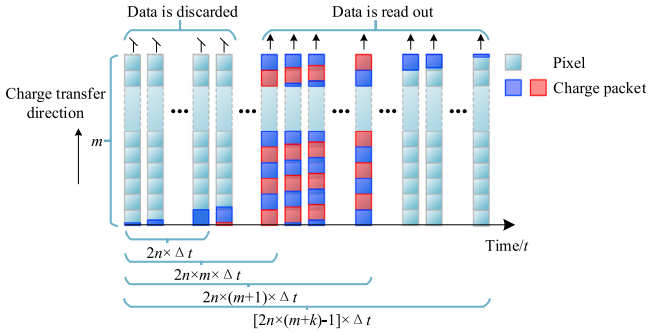


**Fig. 7.** The schematic diagram of the collaborative coding process based on charge transfer and random exposure.

**Table 1**
The values of parameter p that can be selected for different phase number $n$ of TDI CCD.

| $n$ | $p$ | $2n/p$ |
|---|---|---|
| 2 | 1, 2, 4 | 4, 2, 1 |
| 3 | 1, 2, 3, 6 | 6, 3, 2, 1 |
| 4 | 1, 2, 4, 8 | 8, 4, 2, 1 |

the charge transfers $p$ steps corresponding to once exposure. In order to achieve the matching of charge transfer and exposure control, the value of parameter $p$ depends on the phase number $n$ of TDI CCD. Where $p$ can take 1, 2 and 4 for two-phase TDI CCD, $p$ can take 1, 2, 3 and 6 for three-phase TDI CCD, and $p$ can take 1, 2, 4 and 8 for four-phase TDI CCD. The specific correspondences are shown in Table 1.

The $2n/p$ in the above table indicates the number of exposures corresponding to the charge transfer process within one-pixel size range. Therefore, the number of random exposures $S$ during the whole process can be expressed as:

$$S = \frac{2n}{p} \cdot (m + k) - 1. \tag{4}$$

It is assumed that the matrix $E$ for controlling the random exposure of the shutter is:

$$E = \begin{bmatrix} e_1 & e_2 & \cdots & e_{S-1} & e_S \end{bmatrix} \ (e_i = 0, 1). \tag{5}$$

Then according to the above coding process, the measurement matrix $\Phi$ can be expressed as equation given in Box I.

If the original signal is $X$ and the observation result is $Y$, then the whole process can be abstractly expressed as:

$$Y = \Phi X \tag{7}$$

where $X$ is a matrix with $2n \cdot m/p$ rows and 1 column, $Y$ is a matrix with $k$ rows and 1 column, and $\Phi$ is a matrix with $k$ rows and $2n \cdot m/p$ columns. In theory, the imaging resolution can be increased up to $2n/p$ times compared to the traditional method.

Because of the compressed observation, there is $k \le 2n \cdot m/p$, where $k = 2n \cdot m/p$ corresponds to the uncompressed observation. The ratio of the amount of observed data to the mount of original data is defined as the observed compression ratio $D$, which can be expressed as:

$$D = \frac{k \cdot p}{2n \cdot m} \ (0 \le D \le 1). \tag{8}$$

As an important system parameter, the observed compression ratio $D$ determines the total amount of data stored and transmitted by the system, and also has a significant impact on the quality of image restoration.

A column of pixels in the direction of TDI CCD charge transfer is modeled and analyzed above. Other columns are processed in the same way, and then they are integrated into a complete two-dimensional image. It can be seen from the above analysis that the imaging method breaks through the limitation of the Nyquist–Shannon sampling theorem, which subject to the pixel size in traditional imaging and realizes sub-pixel super-resolution imaging. However, it only completes the super-resolution imaging in the one-dimensional direction of the charge transfer, and there is still the traditional imaging mode in the orthogonal direction. Therefore, the obtained image has a one-dimensional image resolution improvement, which provides limited improvement on human visual perception.

## 4. Orthogonal dual detector super-resolution imaging system

In order to achieve the improvement of two-dimensional image resolution, an orthogonal dual detector super-resolution imaging system is proposed based on the above imaging method. The composition and working process of the system are shown in Fig. 8. The system adopts dual TDI CCD detector hardware architecture, of which two detectors are installed perpendicular to each other, and the same target scene is compressed sensing imaging at the same time. The beam splitter divides the target scene into two beams, which are incident on the detector $\alpha$ and detector $\beta$, respectively. The charge transfer and random exposure of the two detectors are achieved through the control and data acquisition circuit, which also completes the acquisition of the two detectors' original image data and transmits them to the upper computer. The image restoration algorithm and two-dimensional image fusion process are mainly accomplished by the upper computer for its powerful computing capability.

The charge transfer of the detector $\alpha$ is performed along the $x$-axis, and the super-resolution imaging in the $x$-axis direction is achieved by the above method. Likewise, the charge transfer of the detector $\beta$ is performed along the $y$-axis, and the super-resolution imaging in the $y$-axis direction is achieved by the above method. After obtaining the super-resolution images in the direction of $x$-axis and $y$-axis respectively, a specific image fusion algorithm is finally required to recover the two-dimensional super-resolution image.

## 5. Two-dimensional image fusion algorithm

Based on the above model, the target scene covered by one-pixel size is taken as the analysis object. The resolution of super-resolution imaging is $4n^2/p^2$, while the number of equations that can be established from one-dimensional super-resolution images in both directions is $4n/p$. Since there is $4n/p \le 4n^2/p^2$, taking the equal sign when $2n/p = 2$, it is necessary but not sufficient problem to merge two orthogonal one-dimensional super-resolution images into a two-dimensional super-resolution image, and there are infinite solutions. Therefore, we need to find a specific image fusion algorithm to optimally recover the two-dimensional super-resolution image.

### 5.1. Convex optimization algorithm

The problem of two-dimensional image fusion can be regarded as image restoration problem in compressed sensing theory, and the super-resolution reconstruction of the image is thus transformed into the convex optimization problem, where the $l_1$ norm method is still used, as shown in Eq. (2). If the super-resolution image data of the target scene covered by a pixel size is integrated into the column vector $X'$, and two one-dimensional super-resolution image data are integrated into the column vector $Y'$, then there is:

$$Y' = \Phi' X' \tag{9}$$

where $X'$ is a matrix with $4n^2/p^2$ rows and 1 column, $Y'$ is a matrix with $4n/p$ rows and 1 column, and $\Phi'$ is a matrix with $4n/p$ rows and $4n^2/p^2$ columns. It is assumed that the element in the matrix $\Phi'$ is $\Phi'_{i,j}$, where $i$ is the row number and $j$ is the column number, which satisfies the following conditions:

$$\boldsymbol{\Phi} = \begin{bmatrix} e_1 + e_2 + \cdots + e_{2n/p} & e_2 + e_3 + \cdots + e_{2n/p+1} & \cdots & e_{2mn/p} + e_{2mn/p+1} + \cdots + e_{(m+1)\cdot 2n/p-1} \\ e_{2n/p+1} + e_{2n/p+2} + \cdots + e_{4n/p} & e_{2n/p+2} + e_{2n/p+3} + \cdots + e_{4n/p+1} & \cdots & e_{(m+1)\cdot 2n/p} + e_{(m+1)\cdot 2n/p+1} + \cdots + e_{(m+2)\cdot 2n/p-1} \\ \vdots & \vdots & \ddots & \vdots \\ e_{(k-1)\cdot 2n/p+1} + e_{(k-1)\cdot 2n/p+2} + \cdots + e_{k\cdot 2n/p} & e_{(k-1)\cdot 2n/p+2} + e_{(k-1)\cdot 2n/p+3} + \cdots + e_{k\cdot 2n/p+1} & \cdots & e_{(m+k-1)\cdot 2n/p} + e_{(m+k-1)\cdot 2n/p+1} + \cdots + e_{(m+k)\cdot 2n/p-1} \end{bmatrix}. \quad (6)$$

**Box I.**

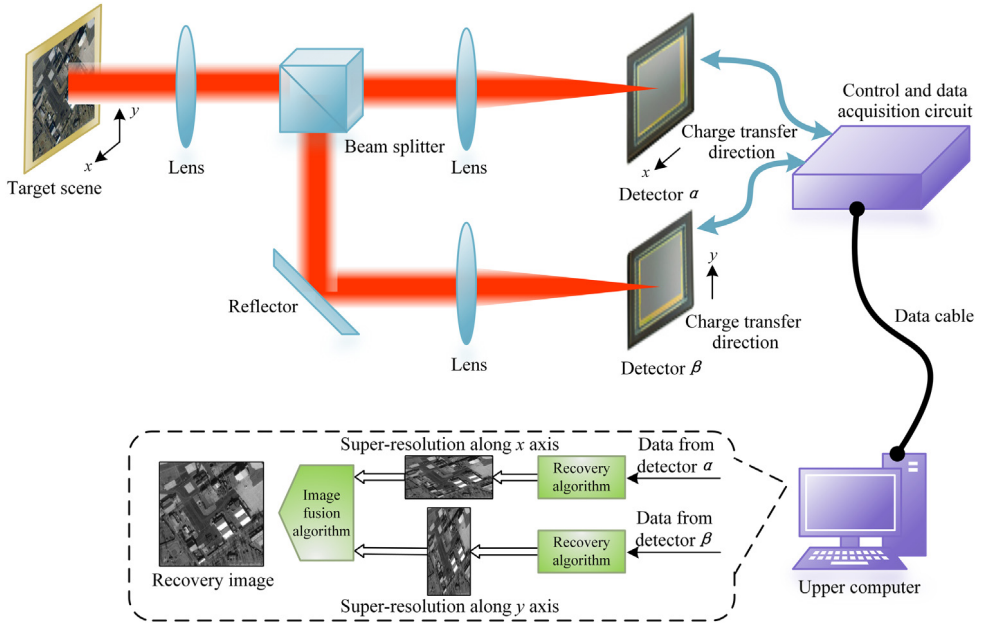


**Fig. 8.** The composition and working process of the orthogonal dual detector super-resolution imaging system.

$$\boldsymbol{\Phi}'_{i,j} = \begin{cases} 1 & (i = 1, j = 1, 2, \ldots, \frac{2n}{p}) \\ 1 & (i = 2, j = \frac{2n}{p} + 1, \frac{2n}{p} + 2, \ldots, \frac{4n}{p}) \\ \vdots & \vdots \\ 1 & (i = \frac{2n}{p}, j = \frac{2n}{p} \times (\frac{2n}{p} - 1) + 1, \frac{2n}{p} \times (\frac{2n}{p} - 1) + 2, \ldots, \frac{4n^2}{p^2}) \\ 1 & (i = \frac{2n}{p} + 1, j = 1, \frac{2n}{p} + 1, \ldots, \frac{2n}{p} \times (\frac{2n}{p} - 1) + 1) \\ 1 & (i = \frac{2n}{p} + 2, j = 2, \frac{2n}{p} + 2, \ldots, \frac{2n}{p} \times (\frac{2n}{p} - 1) + 2) \\ \vdots & \vdots \\ 1 & (i = \frac{4n}{p}, j = \frac{2n}{p}, \frac{4n}{p}, \ldots, \frac{4n^2}{p^2}) \\ 0 & (\text{Others}). \end{cases} \quad (10)$$

For the intuitive expression of the above formula, parameter $2n/p$ is taken as 2 and 3 for instantiation:

$$\boldsymbol{\Phi}' = \begin{bmatrix} 1 & 1 & 0 & 0 \\ 0 & 0 & 1 & 1 \\ 1 & 0 & 1 & 0 \\ 0 & 1 & 0 & 1 \end{bmatrix} (2n/p = 2) \quad (11)$$

$$\boldsymbol{\Phi}' = \begin{bmatrix} 1 & 1 & 1 & 0 & 0 & 0 & 0 & 0 & 0 \\ 0 & 0 & 0 & 1 & 1 & 1 & 0 & 0 & 0 \\ 0 & 0 & 0 & 0 & 0 & 0 & 1 & 1 & 1 \\ 1 & 0 & 0 & 1 & 0 & 0 & 1 & 0 & 0 \\ 0 & 1 & 0 & 0 & 1 & 0 & 0 & 1 & 0 \\ 0 & 0 & 1 & 0 & 0 & 1 & 0 & 0 & 1 \end{bmatrix} (2n/p = 3). \quad (12)$$

Although the matrix $\boldsymbol{\Phi}'$ has the same number of rows and columns at $2n/p = 2$, the matrix is singular at this time, and the convex optimization algorithm is still needed for iterative calculation. Therefore,

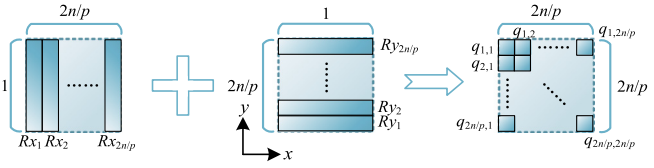


**Fig. 9.** The schematic diagram of the proportional fusion algorithm.

the super-resolution image reconstruction within the pixel is achieved by a specific iterative algorithm of convex optimization, and then the super-resolution images of each pixel are spliced into a complete two-dimensional image.

### 5.2. Proportional fusion algorithm

The image restoration method based on compressed sensing theory is based on the sparse characteristics of natural images. When the target scene covered by one-pixel size is subdivided, the integrity of the image is degraded, which leads to the deterioration of the sparseness, thus resulting in poor results of image restoration.

Based on the similarity of local regions, a proportional fusion algorithm is proposed here. In this method, one dimensional super-resolution imaging data is used as the basic element, and the other one-dimensional data is used as the proportional factor to complete the proportionate distribution of the former.

The schematic diagram of the algorithm is shown in Fig. 9. Still the target scene covered by one-pixel size is taken as the analysis object. The super-resolution imaging data in the $x$-axis and the $y$-axis directions are $R_x$ and $R_y$ respectively, and the grayscale value of each super-resolution


**Fig. 10.** The restored images of Lena. (a) Original image with the resolution of $512 \times 512$. (b) Traditional imaging method with the resolution of $64 \times 64$. (c) Vertical super-resolution restored image with the resolution of $64 \times 384$. (d) Horizontal super-resolution restored image with the resolution of $384 \times 64$. (e) Two-dimensional super-resolution image restored by OMP algorithm with the resolution of $384 \times 384$. (f) Two-dimensional super-resolution image restored by proportional fusion algorithm with the resolution of $384 \times 384$.

point in the figure is $q_{i,j}$ $(i, j = 1 \ldots 2n/p)$. If the data in the direction of the $x$-axis is the basic element, and the data in the direction of the $y$-axis is the proportional factor, the gray value of the super-resolution points is calculated as follows:

$$q_{i,j} = \frac{2n}{p} \cdot Ry_{\frac{2n}{p}-(i-1)} \cdot \frac{Rx_j}{\sum_{m=1}^{\frac{2n}{p}} Rx_m} (i, j = 1 \ldots \frac{2n}{p}). \tag{13}$$

If the data in the direction of the $y$-axis is the basic element, and the data in the direction of the $x$-axis is the proportional factor, the gray value of the super-resolution points is calculated as follows:

$$q_{i,j} = \frac{2n}{p} \cdot Rx_j \cdot \frac{Ry_{\frac{2n}{p}-(i-1)}}{\sum_{m=1}^{\frac{2n}{p}} Ry_m} (i, j = 1 \ldots \frac{2n}{p}). \tag{14}$$

After completing the super-resolution reconstruction of the target scene covered by one-pixel size, other parts are processed in the same way and finally they are spliced into a completed two-dimensional image.

Similar to bilinear interpolation, the algorithm itself does not improve the resolution. However, compared with the traditional bilinear interpolation, this method is based on the super-resolution imaging data that has been acquired by the previous steps. The sub-pixel image information has been contained in the basic data, and the fusion algorithm mainly implements the integration of two-dimensional data. Therefore, it is of significance for super-resolution imaging, which can also be proved in the following simulation results.

## 6. Simulation verification and analysis

The above theoretical model will be verified by the following simulation. The optical system used for experiments works in the visible light band with an f-number of 2. The pixel size of the detector is 30 μm, and the filling factor is 100%. Based on the above system parameters, the influence of the optical diffraction limit can be ignored, and the pixel size of the detector is a determinant of the spatial resolution of the whole system. It is assumed that the pixel numbers $c$ of TDI CCD is 64, the integral numbers $m$ is 64, then the resolution of the target scene in traditional imaging mode is $64 \times 64$ under this condition. If the above super-resolution imaging system is adopted, the corresponding theoretical resolutions are $128 \times 128$, $192 \times 192$, $256 \times 256$, $384 \times 384$ and $512 \times 512$ respectively when $2n/p$ is 2, 3, 4, 6 and 8.

To meet the highest super-resolution parameter requirements, the resolution of the target scene is selected as $512 \times 512$. The quality of super-resolution imaging is evaluated by Peak Signal-to-Noise Ratio(PSNR), Structural Similarity Index (SSIM), and Feature Similarity Index(FSIM) [29–31]. The reference standard was the original image with the resolution of $512 \times 512$.

The full-reference image quality evaluation is based on the same resolution of the restored image and the original image. When the system imaging resolution was lower than that, the nearest neighbor interpolation algorithm will be used to extend to the scale of resolution, wherein orthogonal matching pursuit algorithm (OMP) is adopted in the horizontal and vertical one-dimensional super-resolution restoration algorithm, and it is also adopted in the convex optimization algorithm of two-dimensional image fusion [32–34].

### 6.1. Universal serviceability analysis

In order to fully cover images of different types and features as much as possible, Lena, Mandrill, Peppers, Zebra and two Remote sensing images are selected as target scenes, which can be divided into portraits, scenery and remote sensing images by type. Among them, Mandrill and Zebra contain more texture features, of which Zebra's black and white stripes are the best samples for visually observing super-resolution images. The six images above are selected for simulation, of which $2n/p = 6$ and $D = 0.8$ are taken as preconditions. Based on the set of parameters, the resolution is $64 \times 64$ in traditional imaging mode, and the imaging resolution can reach $384 \times 384$ under the system proposed in this paper. The simulation results are shown in Figs. 10–15.

It can be clearly seen from the simulation results that the system and method proposed in this paper can significantly improve the image resolution, compared with traditional imaging method. For different types of target images, the proportional fusion algorithm is generally superior to the OMP algorithm. Table 2 shows the quantitative results of the restored images with different super-resolution imaging methods, where PF stands for proportional fusion.

From the data in Table 2, we can see that the imaging quality of the system proposed in this paper is better than that of the traditional imaging method, which is consistent with the subjective observations. Moreover, the PSNR, SSIM, and FSIM indexes are consistent in the assessment results of the image quality, so the PSNR will be directly taken as the representation of the image quality evaluation standard in the following text.

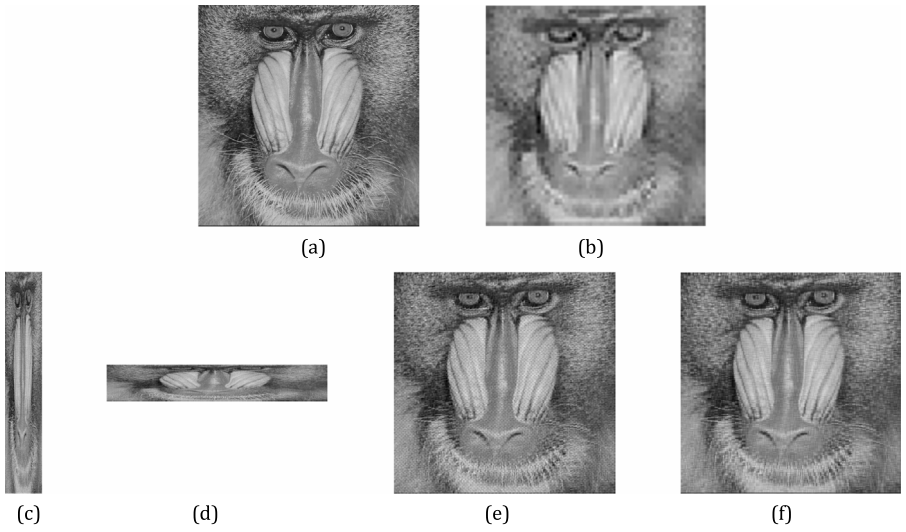


**Fig. 11.** The restored images of Mandrill. (a) Original image with the resolution of 512×512. (b) Traditional imaging method with the resolution of 64×64. (c) Vertical super-resolution restored image with the resolution of $64 \times 384$. (d) Horizontal super-resolution restored image with the resolution of $384 \times 64$. (e) Two-dimensional super-resolution image restored by OMP algorithm with the resolution of $384 \times 384$. (f) Two-dimensional super-resolution image restored by proportional fusion algorithm with the resolution of $384 \times 384$.

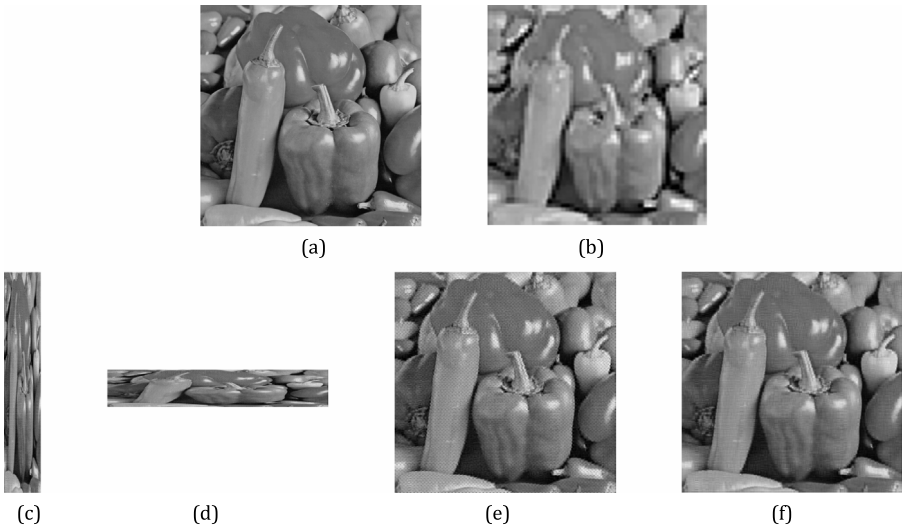


**Fig. 12.** The restored images of Peppers. (a) Original image with the resolution of 512×512. (b) Traditional imaging method with the resolution of 64×64. (c) Vertical super-resolution restored image with the resolution of $64 \times 384$. (d) Horizontal super-resolution restored image with the resolution of $384 \times 64$. (e) Two-dimensional super-resolution image restored by OMP algorithm with the resolution of $384 \times 384$. (f) Two-dimensional super-resolution image restored by proportional fusion algorithm with the resolution of $384 \times 384$.

**Table 2**
The quantitative results of the restored images with different super-resolution imaging methods.

| Images | Traditional imaging method | | | Our method with OMP fusion algorithm | | | Our method with PF fusion algorithm | | |
|---|---|---|---|---|---|---|---|---|---|
| | PSNR | SSIM | FSIM | PSNR | SSIM | FSIM | PSNR | SSIM | FSIM |
| Lena | 25.48 dB | 0.9500 | 0.8412 | 26.21 dB | 0.9569 | 0.8895 | 28.58 dB | 0.9746 | 0.9343 |
| Mandrill | 20.35 dB | 0.8010 | 0.7351 | 21.05 dB | 0.8418 | 0.8744 | 22.08 dB | 0.8708 | 0.9008 |
| Peppers | 25.58 dB | 0.9528 | 0.8488 | 26.29 dB | 0.9590 | 0.8914 | 29.58 dB | 0.9803 | 0.9450 |
| Zebra | 16.43 dB | 0.8652 | 0.7053 | 19.23 dB | 0.9331 | 0.8286 | 20.84 dB | 0.9531 | 0.8801 |
| Remote1 | 22.33 dB | 0.9103 | 0.7790 | 23.95 dB | 0.9389 | 0.8774 | 25.18 dB | 0.9532 | 0.9031 |
| Remote2 | 19.62 dB | 0.8383 | 0.7222 | 21.42 dB | 0.8976 | 0.8643 | 22.32 dB | 0.9153 | 0.8944 |

### 6.2. Parametric analysis

The above simulations are performed only for a specific set of parameters. In the system proposed in this paper, the parameters $2n/p$ and the observed compression ratio $D$ are taken as two significant parameters, and the influence of which on the image quality will be analyzed respectively, based on the image Zebra. Firstly, the influence of observed compression ratio $D$ on image quality is analyzed. When the parameter $2n/p$ is 6, the restored images with different observed compression ratio $D$ are shown in Fig. 16.

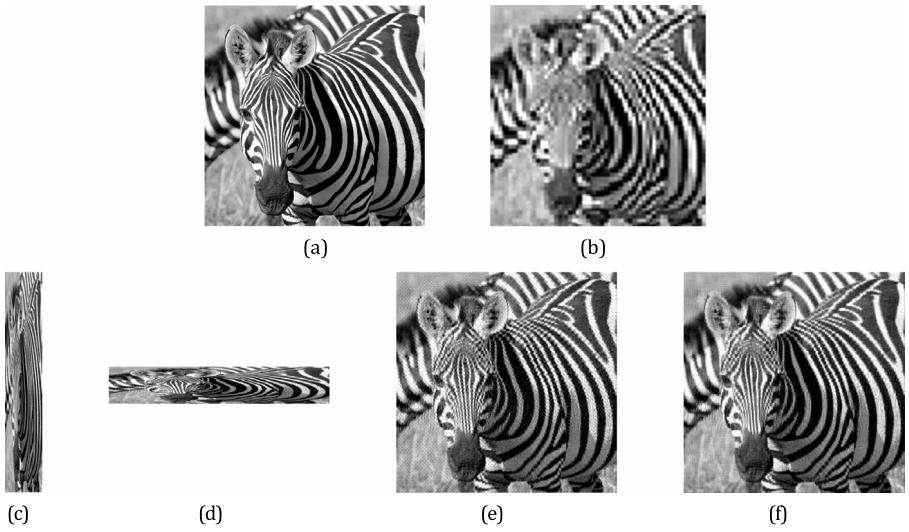


**Fig. 13.** The restored images of Zebra. (a) Original image with the resolution of 512×512. (b) Traditional imaging method with the resolution of 64×64. (c) Vertical super-resolution restored image with the resolution of 64 × 384. (d) Horizontal super-resolution restored image with the resolution of 384 × 64. (e) Two-dimensional super-resolution image restored by OMP algorithm with the resolution of 384 × 384. (f) Two-dimensional super-resolution image restored by proportional fusion algorithm with the resolution of 384 × 384.

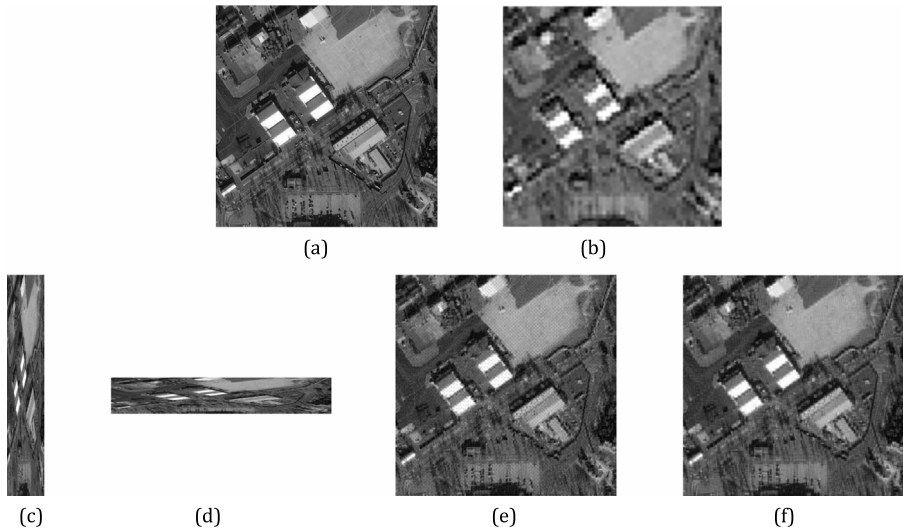


**Fig. 14.** The restored images of Remote1. (a) Original image with the resolution of 512×512. (b) Traditional imaging method with the resolution of 64×64. (c) Vertical super-resolution restored image with the resolution of 64 × 384. (d) Horizontal super-resolution restored image with the resolution of 384 × 64. (e) Two-dimensional super-resolution image restored by OMP algorithm with the resolution of 384 × 384. (f) Two-dimensional super-resolution image restored by proportional fusion algorithm with the resolution of 384 × 384.

It can be seen from the above figure that the image quality is gradually improved with the increase of the observed compression ratio. Furthermore, the relationship between PSNR and observed compression ratio $D$ when $2n/p$ has different values are plotted in Fig. 17, in which OMP stands for orthogonal matching pursuit algorithm, and PF stands for proportional fusion algorithm. From the overall trend, the PSNR is improved with the increase of observed compression ratio $D$, which is due to the greater the $D$, the more the amount of data collected by the system, so that the better quality of restored image is obtained. In general, the PF algorithm is slightly better than that of the OMP fusion algorithm.

Secondly, the influence of parameter $2n/p$ on image quality is also analyzed. When the observed compression ratio $D$ is 0.8, the restored images with different parameter $2n/p$ are shown in Fig. 18.

It can be seen from the above figure that the image quality improves first and then degrades with the increase of $2n/p$. For quantitative analysis, the relationship between PSNR and $2n/p$ when $D$ takes different values is shown in Fig. 19, where the maximum point is obtained when $2n/p$ is 6. The quality of restored image improves with the increase of $2n/p$ generally, which can be explained as the larger the $2n/p$, the greater the theoretical resolution of the system, and the quality of restored image is therefore improved. However, the improvement of image quality slows down with the increase of $2n/p$, and the image quality degrades instead generally when $2n/p$ varies from 6 to 8. On one hand, the increase of $2n/p$ will lead to the improvement of the quality of two one-dimensional super-resolution images. On the other hand, in the process of two-dimensional image fusion, more data needs to be recovered with less data with the increase of $2n/p$,

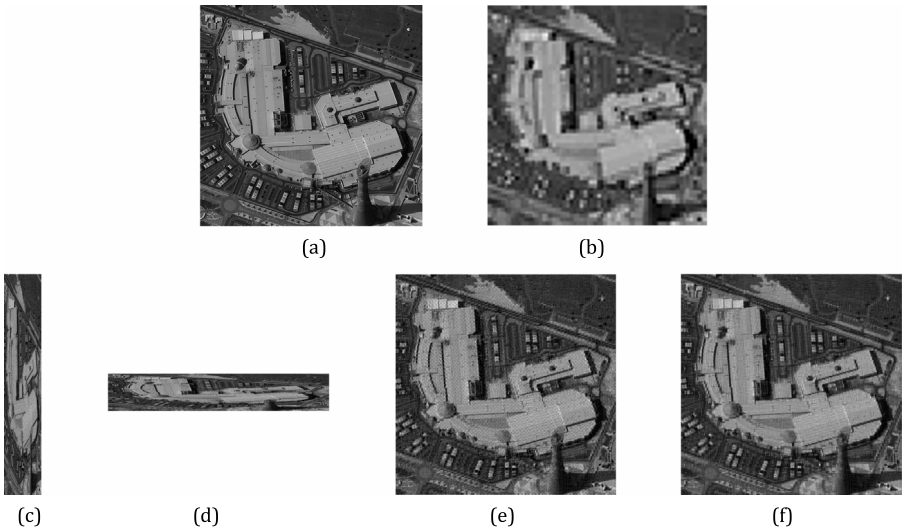


**Fig. 15.** The restored images of Remote2. (a) Original image with the resolution of 512×512. (b) Traditional imaging method with the resolution of 64×64. (c) Vertical super-resolution restored image with the resolution of $64 \times 384$. (d) Horizontal super-resolution restored image with the resolution of $384 \times 64$. (e) Two-dimensional super-resolution image restored by OMP algorithm with the resolution of $384 \times 384$. (f) Two-dimensional super-resolution image restored by proportional fusion algorithm with the resolution of $384 \times 384$.

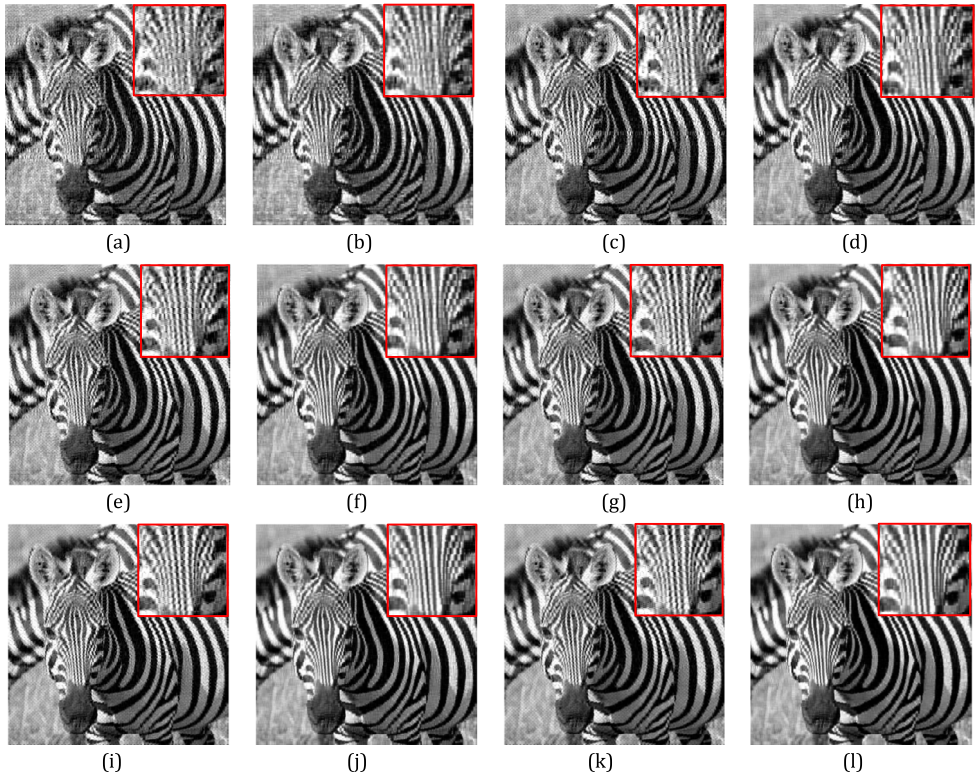


**Fig. 16.** The simulation results with different compression ratio $D$. (a) $D = 0.4$ with OMP algorithm. (b) $D = 0.4$ with PF algorithm. (c) $D = 0.5$ with OMP algorithm. (d) $D = 0.5$ with PF algorithm. (e) $D = 0.6$ with OMP algorithm. (f) $D = 0.6$ with PF algorithm. (g) $D = 0.7$ with OMP algorithm. (h) $D = 0.7$ with PF algorithm. (i) $D = 0.8$ with OMP algorithm. (j) $D = 0.8$ with PF algorithm. (k) $D = 0.9$ with OMP algorithm. (l) $D = 0.9$ with PF algorithm.

resulting in a degradation in the quality of restored image. Due to the comprehensive effect of the above two factors, the quality of restored image improves first and then degrades with the increase of $2n/p$.

The imaging system based on compressed sensing theory proposed in this paper needs the optimized iterative algorithm in the process of image restoration, so we must consider the consumption time of image restoration, so as to objectively evaluate the real-time performance of the system. Fig. 20 indicates that the system time-consuming increases with the increase of the parameters $2n/p$ and $D$. Therefore, improving the image quality by increasing the values of $2n/p$ and $D$ will inevitably lead to an increase in the time-consuming of the system, resulting in a decrease in real-time performance. Therefore, comprehensive consideration is required in practical applications.

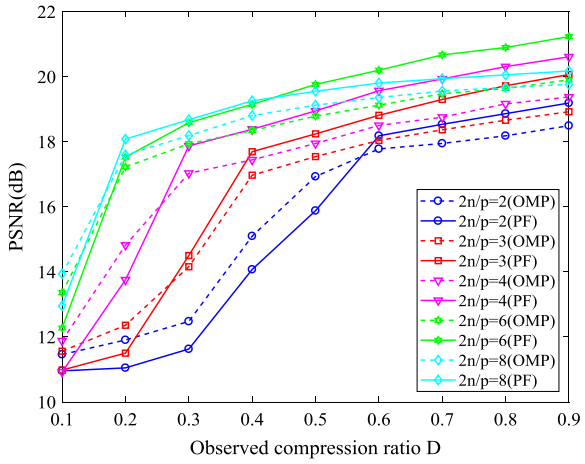


**Fig. 17.** The relationship between PSNR and observed compression ratio $D$ in different $2n/p$.

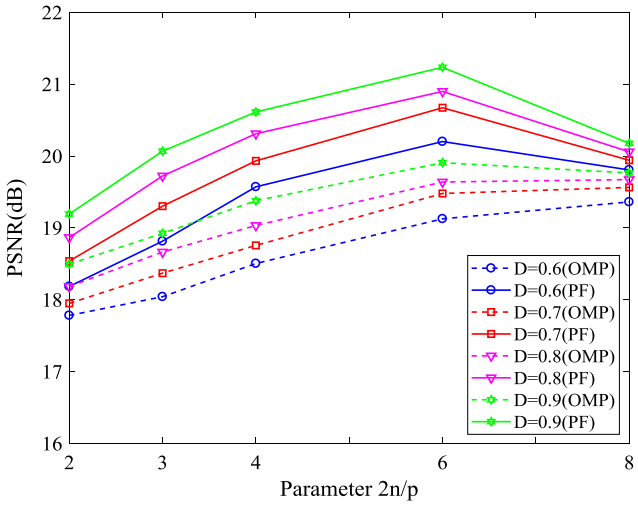


**Fig. 19.** The relationship between PSNR and $2n/p$ when $D$ takes different values.

### 6.3. Optimization analysis of data quantity

With the improvement of restored image quality, the total amount of data collected by the system increases gradually, which further aggravates the data storage and transmission pressure of the system. Therefore, it is significant to analyze how to obtain higher image quality with a limited amount of data. It is assumed that the total amount of data collected by the system in the super-resolution imaging process is $D_t$, which can be expressed as:

$$D_t = 2 \cdot c \cdot k = 2 \cdot c \cdot m \cdot D \cdot \frac{2n}{p} \tag{15}$$

where there is $c = 64$ and $m = 64$ under the current simulation parameters. It can be seen from the above equation that the observed compression ratio $D$ is inversely proportional to $2n/p$ on the premise that the total amount of data $D_t$ is fixed. Taking image Zebra as the example, the PSNR of restored image with different $D_t$ are shown in Table 3, of which the amount of data $D_t$ ranges from 14 746 to 58 982, and "/" indicates that there is no such situation.

As a whole, the PSNR of the restored image increases with the increase of $D_t$. In the same amount of data, the smaller the $2n/p$, the higher the PSNR. However, because of the limitation of the observed compression ratio $D$, the smaller the $2n/p$, the lower the maximum

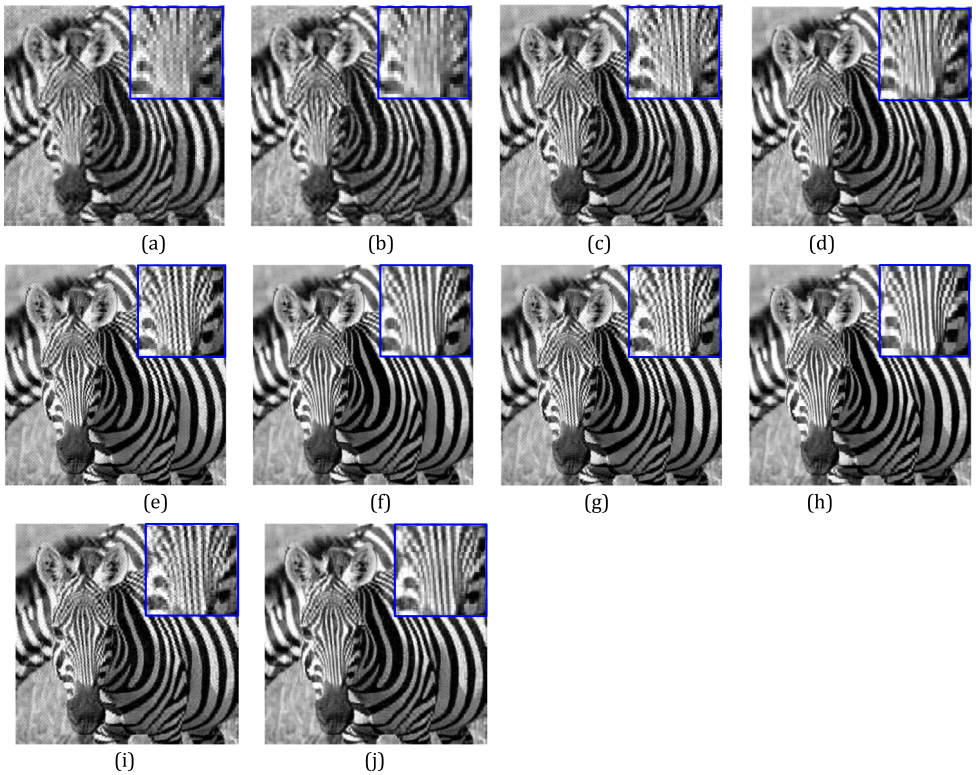


**Fig. 18.** The simulation results with different parameter $2n/p$. (a) $2n/p = 2$ with OMP algorithm. (b) $2n/p = 2$ with PF algorithm. (c) $2n/p = 3$ with OMP algorithm. (d) $2n/p = 3$ with PF algorithm. (e) $2n/p = 4$ with OMP algorithm. (f) $2n/p = 4$ with PF algorithm. (g) $2n/p = 6$ with OMP algorithm. (h) $2n/p = 6$ with PF algorithm. (i) $2n/p = 8$ with OMP algorithm. (j) $2n/p = 8$ with PF algorithm.

**Table 3**
The PSNR of the restored images with different $D_t$ and $2n/p$ combinations(dB).

| $D_t$ | Fusion algorithm | $2n/p = 2$ | $2n/p = 3$ | $2n/p = 4$ | $2n/p = 6$ | $2n/p = 8$ |
|---|---|---|---|---|---|---|
| | | $D = 0.9$ | $D = 0.6$ | $D = 0.45$ | $D = 0.3$ | $D = 0.225$ |
| 14 746 | OMP | 18.50 | 18.04 | 17.70 | 17.94 | 17.62 |
| | PF | 19.19 | 18.82 | 18.67 | 18.59 | 17.98 |
| | | / | $D = 0.9$ | $D = 0.675$ | $D = 0.45$ | $D = 0.3375$ |
| 22118 | OMP | / | 18.92 | 18.74 | 18.57 | 18.30 |
| | PF | / | 20.07 | 19.88 | 19.46 | 18.77 |
| | | / | / | $D = 0.9$ | $D = 0.6$ | $D = 0.45$ |
| 29491 | OMP | / | / | 19.38 | 19.13 | 18.97 |
| | PF | / | / | 20.61 | 20.20 | 19.41 |
| | | / | / | / | $D = 0.9$ | $D = 0.675$ |
| 44237 | OMP | / | / | / | 20.60 | 19.66 |
| | PF | / | / | / | 21.24 | 20.07 |
| | | / | / | / | / | $D = 0.9$ |
| 58982 | OMP | / | / | / | / | 19.76 |
| | PF | / | / | / | / | 20.18 |

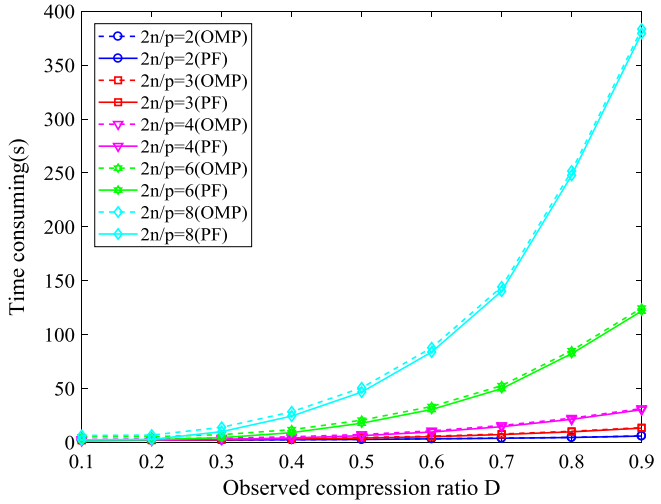


**Fig. 20.** The relationship between time-consuming and observed compression ratio $D$ when $2n/p$ takes different values.

amount of data that can be selected. Therefore, a larger $2n/p$ and a larger $D_t$ are required to obtain a higher PSNR in general. But in particular, the maximum point in the table is located at $D_t = 44\,237$, $2n/p = 6$, and it has been explained in the above analysis.

## 7. Conclusions

Based on compressed sensing theory, a collaborative coding method based on TDI CCD charge transfer and random exposure is proposed in this paper, which breaks through the limitation of pixel size and achieves the improvement of one-dimensional image resolution. By expanding the above method, an orthogonal dual detector super-resolution imaging system is established, which realizes the improvement of two-dimensional image resolution. In the part of two-dimensional image fusion algorithm, we propose the convex optimization algorithm and the proportional fusion algorithm. The simulation results show that the imaging system can indeed improve the quality of two-dimensional image, and the image quality of the proportional fusion algorithm is slightly better than that of the convex optimization algorithm. From the overall trend, the quality of restored image improves with the increase of observed compression ratio. And in the same amount of data, the smaller the subdivision, the higher the image quality. The proposed method and system provide an innovative approach of system implementation for super-resolution imaging based on compressed sensing theory.

## Acknowledgment

This work is supported by Technology Innovation and Achievement Transformation Project of Jilin Province of China (Grant No. 20150312039ZG).

## References

[1] Emmanuel J. Candès, Justin Romberg, Terence Tao, Robust uncertainty principles: Exact signal reconstruction from highly incomplete frequency information, IEEE Trans. Inform. Theory 52 (2006) 489–509.
[2] David L. Donoho, Compressed sensing, IEEE Trans. Inform. Theory 52 (2006) 1289–1306.
[3] Emmanuel J. Candès, Justin Romberg, Sparsity and incoherence in compressive sampling, Inverse Problems 23 (2006) 969–985.
[4] Emmanuel J. Candès, Michael B. Wakin, An introduction to compressive sampling, IEEE Signal Process. Mag. 25 (2008) 21–30.
[5] Joel A. Tropp, Jason N. Laska, Marco F. Duarte, Justin K. Romberg, Richard G. Baraniuk, Beyond nyquist: Efficient sampling of sparse bandlimited signals, IEEE Trans. Inform. Theory 56 (2010) 520–544.
[6] Wangli Hao, Meng Han, Wangbao Hao, Compressed sensing remote sensing image reconstruction based on wavelet tree and nonlocal total variation, in: Proceedings of IEEE International Conference on Network and Information Systems for Computers, ICNISC, 2016, pp. 317–322..
[7] Christian G. Graff, Emil Y. Sidky, Compressive sensing in medical imaging, Appl. Opt. 54 (2015) C23–C44.
[8] Y.C. Eldar, Compressed sensing and applications to optical imaging, in: Frontiers in Optics 2012/Laser Science XXVIII, OSA Technical Digest (Online), Optical Society of America, 2012, paper FM4C.1.
[9] Quan Dong, Li Cai, Shunan Wang, Peng Zhang, Hong Wang, Lin Shi, Zhengsheng Wang, Compressed sensing based aperture encoded imaging radar technique, in: Proceedings of IEEE International Conference on Radar, RADAR, 2016, pp. 1–4..
[10] Marco F. Duarte, Mark A. Davenport, Dharmpal Takhar, Jason N. Laska, Ting Sun, Kevin F. Kelly, Richard G. Baraniuk, Single-pixel imaging via compressive sampling, IEEE Signal Process. Mag. 25 (2008) 83–91.
[11] Qi Tong, Yilin Jiang, Haiyan Wang, Limin Guo, Image reconstruction of dynamic infrared single-pixel imaging system, Opt. Commun. 410 (2018) 35–39.
[12] John P. Dumas, Muhammad A. Lodhi, Waheed U. Bajwa, Mark C. Pierce, Computational imaging with a highly parallel image-plane-coded architecture: challenges and solutions, Opt. Express 24 (2016) 6145–6155.
[13] A.C. Sankaranarayanan, A. Veeraraghavan, Parallel compressive imaging, in: Imaging and Applied Optics 2015, OSA Technical Digest (Online), Optical Society of America, 2015, paper CTh3E.4.
[14] Wen-Kai Yu, Xu-Ri Yao, Xue-Feng Liu, Long-Zhen Li, Guang-Jie Zhai, Three-dimensional single-pixel compressive reflectivity imaging based on complementary modulation, Appl. Opt. 54 (2015) 363–367.
[15] Liang Gao, Jinyang Liang, Chiye Li, Lihong V. Wang, Single-shot compressed ultrafast photography at one hundred billion frames per second, Nature 516 (2014) 74–77.
[16] L. Jacques, P. Vandergheynst, A. Bibet, V. Majidzadeh, A. Schmid, Y. Leblebici, CMOS compressed imaging by random convolution, in: Proceedings of IEEE International Conference on Acoustics, Speech and Signal Processing, ICASSP, 2009, pp. 1113–1116..

[17] Huixian Ye, Li Tian, Qi Zhang, Hui Wang, Songlin Feng, CMOS image sensor with programmable compressed sensing, in: Proceedings of IEEE 11th International Conference on ASIC, ASICON, 2015, pp. 1–4..
[18] Jun Tanida, Ryoichi Horisaki, Computational imaging based on multi-aperture optics, Proc. SPIE 9659 (2015) 965905.
[19] Patrick Llull, Xuejun Liao, Xin Yuan, Jianbo Yang, David Kittle, Lawrence Carin, Guillermo Sapiro, David J. Brady, Coded aperture compressive temporal imaging, Opt. Express 21 (2013) 10526–10545.
[20] Yueting Chen, Chaoying Tang, Zhihai Xu, Qi Li, Min Cen, Huajun Feng, Adaptive reconstruction for coded aperture temporal compressive imaging, Appl. Opt. 56 (2017) 4940–4947.
[21] Pawan K. Baheti, Mark A. Neifeld, Compressive imaging using random active illumination, in: Frontiers in Optics 2007/Laser Science XXIII/Organic Materials and Devices for Displays and Energy Conversion, OSA Technical Digest (CD), Optical Society of America, 2007, paper FThQ2.
[22] Milad I. Akhlaghi, Aristide Dogariu, Compressive correlation imaging with random illumination, Opt. Lett. 40 (2015) 4464–4467.
[23] E. Mojica, S. Pertuz, H. Arguello, High-resolution coded-aperture design for compressive X-ray tomography using low resolution detectors, Opt. Commun. 404 (2017) 103–109.
[24] M. Marquez, Y. Mejia, H. Arguello, Compressive spectral image super-resolution by using singular value decomposition, Opt. Commun. 404 (2017) 163–168.
[25] Guangming Shi, Dahua Gao, Xiaoxia Song, Xuemei Xie, Xuyang Chen, Danhua Liu, High-resolution imaging via moving random exposure and its simulation, IEEE Trans. Image Process. 20 (2011) 276–282.
[26] Dejiang Wang, Wenming Li, Yuan Yao, Houtian Huang, Yutang Wang, A fine image motion compensation method for the panoramic TDI CCD camera in remote sensing applications, Opt. Commun. 298–299 (2013) 79–82.
[27] Wenyi Ren, Qizhi Cao, Dan Wu, Jiangang Jiang, Guoan Yang, Yingge Xie, Guodong Wang, Sheqi Zhan, Bi-dimensional empirical mode decomposition based fringe-like pattern suppression in polarization interference imaging spectrometer, Opt. Commun. 407 (2018) 280–284.
[28] Bianhong Zhao, Bin He, Destriping of TDI-CCD remote sensing image, in: 2010 3rd International Conference on Advanced Computer Theory and Engineering, ICACTE, 6, 2010, pp. 325–328..
[29] S. Vishnukumar, M. Wilscy, Single image super-resolution based on compressive sensing and improved TV minimization sparse recovery, Opt. Commun. 404 (2017) 80–93.
[30] Z. Wang, A.C. Bovik, H.R. Sheikh, E.P. Simoncelli, Image quality assessment: from error visibility to structural similarity, IEEE Trans. Image Process. 13 (2004) 600–612.
[31] Lin. Zhang, Lei. Zhang, X. Mou, D. Zhang, FSIM: A feature similarity index for image quality assessment, IEEE Trans. Image Process. 20 (2011) 2378–2386.
[32] Joel A. Tropp, Anna C. Gilbert, Signal recovery from random measurements via orthogonal matching pursuit, IEEE Trans. Inform. Theory 53 (2007) 4655–4666.
[33] Sujit Kumar Sahoo, Anamitra Makur, Signal recovery from random measurements via extended orthogonal matching pursuit, IEEE Trans. Signal Process. 63 (2015) 2572–2581.
[34] Ehsan Miandji, Mohammad Emadi, On probability of support recovery for orthogonal matching pursuit using mutual coherence, IEEE Signal Process. Lett. 24 (2017) 1646–1650.